Current Optics and Photonics
Vol. 5, No. 1, February 2021, pp. 16–22

ISSN: 2508-7266(Print) / ISSN: 2508-7274(Online)
DOI: https://doi.org/10.3807/COPP.2021.5.1.016

Shannon Entropy as an Indicator of the Spatial Resolutions of the Morphologies of the Mode Patterns in an Optical Resonator

Kyu-Won Park[1]*, Jinuk Kim[1], and Songky Moon[2]

[1]Department of Physics and Astronomy & Institute of Applied Physics, Seoul National University, Seoul 08826, Korea
[2]Faculty of Liberal Education, Seoul National University, Seoul 08826, Korea

(Received August 26, 2020 : revised November 17, 2020 : accepted November 28, 2020)

We present the Shannon entropy as an indicator of the spatial resolutions of the morphologies of the resonance mode patterns in an optical resonator. We obtain each optimized number of mesh points, one of minimum size and the other of maximum one. The optimized mesh-point number of minimum size is determined by the identifiable quantum number through a chi-squared test, whereas the saturation of the difference between Shannon entropies corresponds to the other mesh-point number of maximum size. We also show that the optimized minimum mesh-point increases as the (real) wave number increases and approximates the proportionality constant between them.

Keywords : Shannon entropy, Optical resonator, Boundary element method, Spatial resolution
OCIS codes : (100.5010) Pattern recognition; (140.3410) Laser resonators; (330.6100) Spatial discrimination; (330.6130) Spatial resolution; (350.5730) Resolution

I. INTRODUCTION

Optical resonators have been considered good candidates for optical sources [1, 2] and have been studied extensively in various theoretical and experimental contexts, such as unidirectional emission [3–5], high quality factors [6, 7], optical sensors [8, 9], and whispering gallery modes [10–12]. They are also regarded as good platforms for studying many fundamental physical phenomena, *e.g.* ray-way correspondence [13, 14], tunneling [15, 16], scar [17, 18], avoided crossing [19, 20], exceptional points [21, 22], and chaos [23, 24]. Furthermore, in previous work [25] we first showed that the Shannon entropy can also be investigated in microcavities.

The Shannon entropy, first introduced by Shannon, is a functional that measures the average information content of a statistical ensembles of a random variable. It was originally developed and utilized in communication theory [26] and statistical mechanics [27], but recently it has been also exploited in various areas. The Shannon entropy has been used not only for molecular descriptors [28], protein sequences [29] in bio-systems and algorithmic complexity [30] in information theory, but also for avoided crossing in optics: the relation of which to the Shannon entropy has been investigated for microcavities [25], atomic physics [31, 32], and the quantum transition from order to chaos in quantum chaos [33].

In a previous study [25], we showed that the Shannon entropy changes depending on the parameter and is maximized at the center of the interaction, owing to a coherent superposition of wavefunctions (mixing of the wavefunctions), which indicates that the variation of the Shannon entropy is related to the variation of the morphologies of the wavefunctions. This fact suggests that the Shannon entropy can be used to study the morphology of the wavefunction. In this paper, we employ the Shannon entropy to determine the optimal number of mesh points for the morphology of the mode pattern in a two-dimensional elliptical optical resonator.

In the case of the one-dimensional resolution of the

*Corresponding author: wind999@snu.ac.kr, ORCID 0000-0002-4933-9799

Color versions of one or more of the figures in this paper are available online.

boundary-element method, the optimized boundary line element ΔS_{opt} for the relevant wavelength λ_{res} is approximated by $\Delta S_{opt} \sim 16\lambda_{res}$ [34]. Thus, when $\Delta S \leq \Delta S_{opt}$, the two-dimensional resolution (the morphology of the mode pattern) depends on the discretization of the area in the resonator. Specifying the spatial resolution of the morphology is inevitable in numerical calculations since we must discretize the object [34]; hence, estimating the optimized spatial resolution can reduce any unnecessary effort in numerical calculations. To the best of our knowledge, however, no method has been devised for estimating the optimized resolution of the mode pattern in an optical resonator with the boundary-element method.

This paper is organized as follows. In Section II, the Shannon entropy of an elliptical microcavity is introduced. In Section III, we study the difference between Shannon entropies and its saturation. Comparison of two Shannon entropies for spatial resolution is discussed in Section IV. Finally, we summarize our work in Section V.

II. THE SHANNON ENTROPY OF AN ELLIPTICAL MICROCAVITY

The eigenvalue trajectories of an elliptical resonator with major axis a and minor axis b are shown in Fig. 1. The eigenvalues and eigenmodes are calculated using the boundary-element method (BEM) [34] with a refractive index of the resonator $n = 3.3$ for the TE mode. The BEM is useful for obtaining the eigenvalues and eigenmodes in various areas such as bubble dynamics [35], scattering of broadband waves [36], and modeling of over-moded cavities [37]. The real and imaginary parts of the eigenvalues kR are plotted as the eccentricity $\varepsilon = \sqrt{1-\left(\frac{b}{a}\right)^2}$ from $\varepsilon = 0.0$ to $\varepsilon = 0.51$ in Figs. 1(a) and 1(b), respectively. In this paper, we consider only the inner part of the resonator, which a non-Hermitian Hamiltonian Heff describes well [38, 39]. That is

$$H_{eff}\,\psi_k = z_k\psi_k, \tag{1}$$

with its complex eigenvalues z_k and their eigenfunctions ψ_k. Here, the complex eigenvalues are defined by $z_k = E_k - \frac{i}{2}\Gamma_k$ with the real part E_k and imaginary part Γ_k representing an energy and a decay width of k-the eigenmodes, respectively, resulting in a quality factor $Q = \frac{E_k}{\Gamma_k}$.

To introduce the discrete probability distribution, we discretize the area within the resonator into the N pieces that play the role of the N-mesh points. Then we assign the probability density ($\rho = |\psi|^2$) to each mesh point r_j under the normalization condition $\sum_{j=1}^{N}\rho(r_j) = 1$ by interpreting the N-mesh points as the 1 spatial-coordinate states. With this discrete probability distribution $\rho(r_j)$, we can easily obtain the discrete Shannon entropy for the N mesh points or the N spatial-coordinate states defined by

$$S(\rho) \equiv -\sum_{j=1}^{N}\rho(r_j)\log\rho(r_j). \tag{2}$$

We obtain several Shannon entropies by the definition above. In Fig. 1, the Shannon entropies for $N = 98$, 212, 398, 596, 810, and 1040 are shown in panels (c), (d), (e), (f), (g), and (h) respectively. Note that not only do the profiles

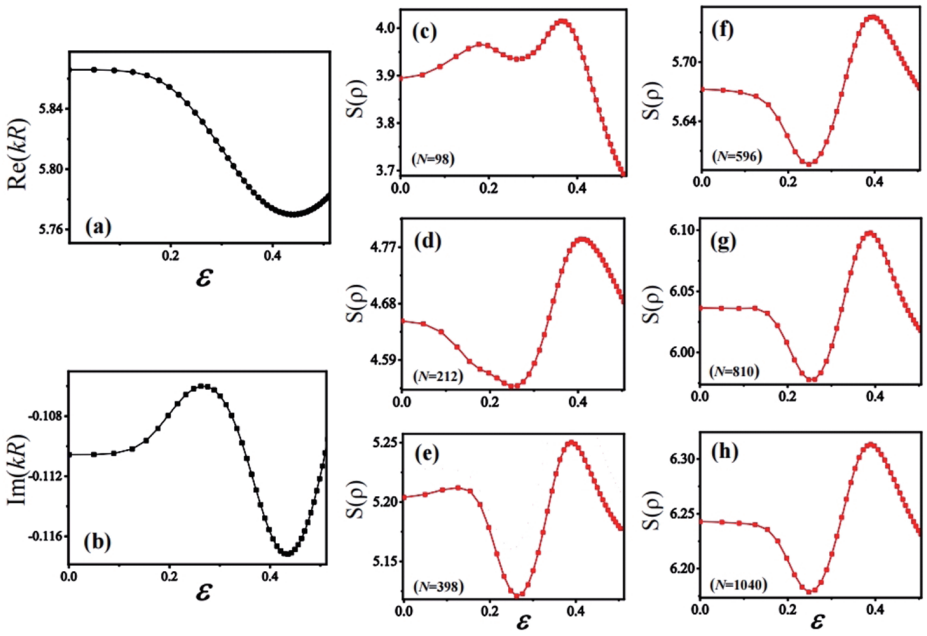

FIG. 1. The eigenvalue trajectories and their corresponding Shannon entropies. (a) Real part of eigenvalues kR as the eccentricity ε is varied. (b) Imaginary part of eigenvalues kR as ε is varied. The Shannon entropies for $N = 98$, 212, 398, 596, 810, and 1040 are shown in (c), (d), (e), (f), (g), and (h), respectively.

of the Shannon entropies vary, but also their absolute values. *i.e.*, the values increase with increasing N mesh points.

We can understand this behavior by considering maximal entropy states. The maximal entropy with N mesh points is given by $S(\rho_{\max})=\log N$. Since the state for the maximal entropy is not the eigenstate of a Hamiltonian, we artificially impose uniform intensities inside the resonator.

III. DIFFERENCE BETWEEN SHANNON ENTROPIES AND ITS SATURATION

In this section, we consider the Shannon entropies for resonance mode patterns and maximal entropies simultaneously as functions of N mesh points and the results are shown in Fig. 2(a). The curved lines are Shannon entropies for resonance mode patterns, whereas the straight lines are maximal entropies. These lines are too complicated to understand since two types of the Shannon entropies seem to behave independently. However, we can reveal the properties of these behaviors by considering the differences between these two types of Shannon entropies.

To study the behavior of Shannon entropies depending on a specific N value, let us consider the differences between the Shannon entropies of the specific mode patterns $S(\rho)$ and maximal entropies $S(\rho_{max})$

$$D_{\mathrm{SE}}(N) \equiv \log N - S(\rho). \tag{3}$$

Note that Eq. (3) is equivalent to a Kullback-Leibler divergence when one of the two probability distributions is uniform, i.e., $D_{\mathrm{KL}}(\mu \parallel \nu) = -\sum_{j=1}^{N} \mu(r_j)\log\frac{\nu(r_j)}{\mu(r_j)}$ where $\nu(r_j) = \frac{1}{N}$ [40]. The results are shown in Fig. 2(b). They have maximum values at $\varepsilon \simeq 0.25$ and minimum values at $\varepsilon \simeq 0.38$, respectively, and they have simpler forms than the Shannon entropies themselves. Furthermore, it should be noted that the D_{SE} curves fluctuate below $N_{(4)} = 2020$ but almost saturate beyond the $N_{(4)} = 2020$. The inset in Fig. 2(b) clearly shows this behavior. For our numerical cut off, we consider on the order of 10^{-6} for D_{SE}. Thus, the saturated curve for D_{SE} (N) can be defined by the value of D_{SE} $(N_{(m+1)})$ − D_{SE} $(N_{(m)})$ whose order is 10^{-6}. The value D_{SE} $(N_{(7)})$ − D_{SE} $(N_{(6)}) \approx 8 \times 10^{-6}$. In this way, we adopt the D_{SE} $(N_{(7)}) = 3492$ as the saturated curve for the difference between the Shannon entropies.

IV. COMPARISON OF TWO SHANNON ENTROPIES FOR SPATIAL RESOLUTION

4.1. Theoretical and Observed Values for Spatial Resolution

The Kullback-Leibler divergence is directly related to the difference in Shannon entropies when one of the two probability distributions is uniform, but in general this is not the case. Instead we employ the chi-squared test, which can be defined as an approximation of a Kullback-Leibler divergence [41]. The chi-squared test is used to quantify a difference between expected and observed values in a data set [42]. Its definition is

$$\chi^2 = \sum_{i=1}^{\tilde{n}} \frac{(O_i - E_i)^2}{E_i}, \tag{4}$$

where O are the observed values actually obtained, E are the expected or theoretical values assumed to be true, and $\tilde{n}$ is the number of cells.

Actually, it is the statistical procedures whose results are evaluated with reference to the chi-squared distribution.

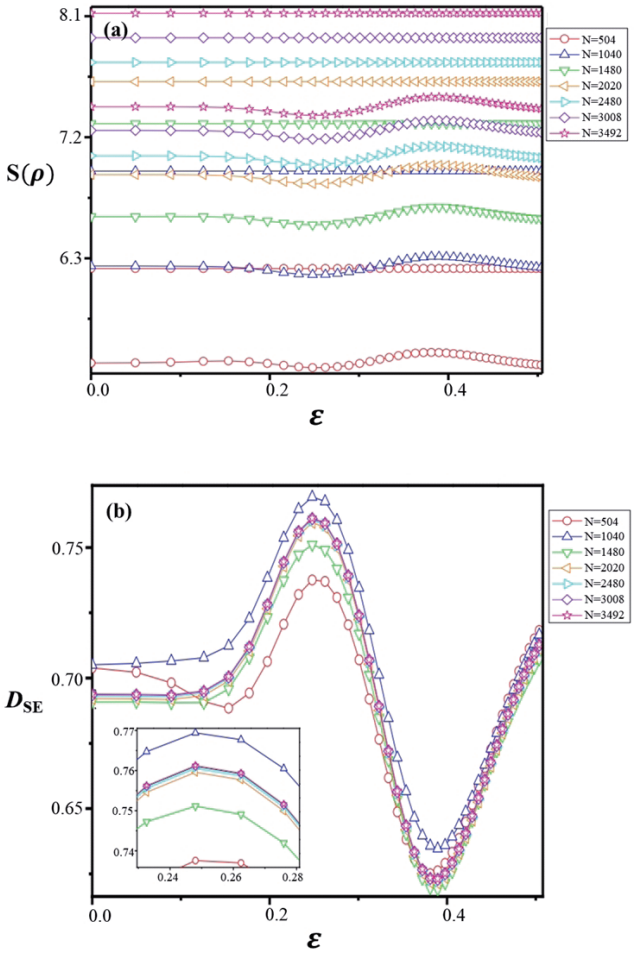

FIG. 2. Saturation of Shannon entropy. (a) The Shannon entropies for mode patterns and maximal entropies as the number of mesh point N is varied. The curved lines are Shannon entropies for the probability density of the resonance mode pattern whereas the straight lines are maximal entropies. The red circles are for N = 504, the blue up-ward triangles are for N = 1040, the green down-ward triangles are for N = 1480, the orange left-facing triangles are for N = 2020, the cyan right-facing triangles are for N = 2480, the violet diamonds are for N = 3008, and the pink stars are for N = 3492. (b) Differences between the two types of entropies in (a) are shown. D_{SE} shows a tendency toward saturated behavior past $N_{(4)} = 2020$. The inset clearly shows this behavior.

However, we take advantage of Eq. 4 to quantify the differences between two data sets, even though our data sets were not evaluated with reference to the chi-squared distribution. Here we suggest that the observed values of the Shannon entropy as a function of a specific N are given by Eq. (2), *i.e.* the Shannon entropy of the specific mode patterns are obtained at N when N is less than the saturated number $N_{(7)}$ = 3492, and the expected values are given by the difference between the maximal entropies for the specific N and the saturated curve D_{SE} (N = 3492). That is, $E(N) \equiv \log N - D_{SE}$ (N = 3492).

In our case, it should be also noticed that the number of unit cells $\tilde{n}$ corresponds to the number of discretized coordinates ε. In Fig. 3 red squares indicate the observed values and blue circles the expected values. In Figs. 3(a), (b), (c), (d), (e), and (f), we see the observed and expected values in sequence, depending on each number N of mesh points: 98, 212, 398, 596, 810, and 1040. Note that the absolute values of the two curves (red and blue) increase as N increases. Furthermore, the profiles of two different colored curves become similar to each other as N increases. This similarity between the two different curves (data) can be quantified by the value of the chi-squared test χ^2.

4.2. Chi-squared Test and Spatial Resolution of Mode Patterns in a Resonator

The results of the chi-squared test, which are obtained from the observed and theoretical values shown in Fig. 3, are presented in Fig. 4. The red squares for the chi-squared values are shown as a function of the N mesh points. Note that χ^2 decreases drastically when $N \leq 800$ and gradually when $N \geq 800$. The decay rate of the curve at point A (N = 212) is much larger than at point B (N = 810), *i.e.* the slope at A is steep but that at B converges critically to zero. This fact suggests that the value at B (N = 810) can be used to estimate an optimized minimum-mesh point for a mode pattern.

To manifest this suggestion, we plot the mode patterns at each number of mesh points in Fig. 4. We can expect that the morphologies of the mode patterns become clear as N increases. The morphologies in the A group are so blurred that we cannot recognize the mode patterns. Then, let us examine the morphologies in the B and C groups. First of all, it should be noticed that the morphology of C_1 features clear quantum numbers such as radial number l = 5 and angular number m = 3 at ε = 0. Also, C_1 and C_2 have smooth morphologies. We chose the eccentricity values ε = 0.25 and 0.38 to be the extremal points of Shannon entropy in our examples. In addition, these extremal points are related to mode-pattern localization or delocalization. That is, the mode pattern is well localized at ε = 0.25 as a bouncing-ball-type mode, resulting in minimal Shannon entropy. On the contrary, the mode pattern at ε = 0.38 is delocalized, since it is the transient mode from the bouncing-ball to another mode (not shown), and consequently results in maximal Shannon entropy. Our future work will deal with wave localization and delocalization, comparing to the inverse participation ratio [43, 44]. Next, let us compare the morphologies of $C_{1,2,3}$ to those of $B_{1,2,3}$. We can (barely) identify the quantum numbers (l = 5, m = 3) in B_1 as well as in C_1, and the other two overall morphologies of $B_{1,2}$ are similar to those of $C_{1,2}$, even though their resolutions are quite differ-

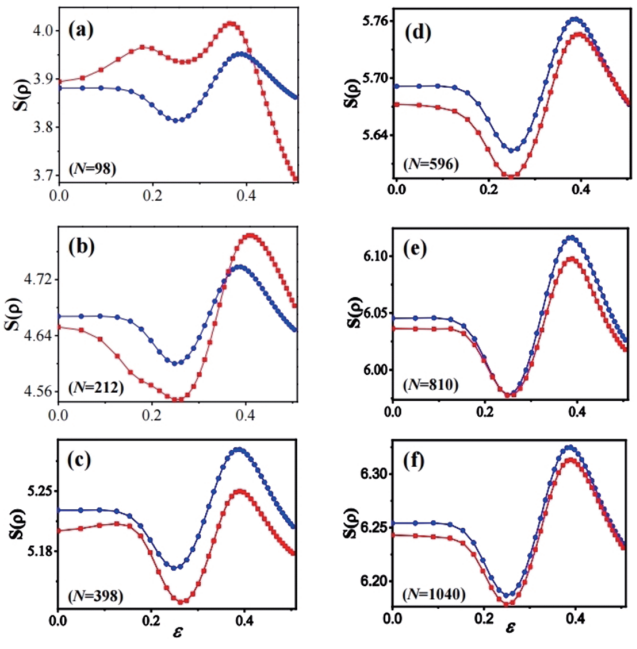

FIG. 3. Observed and expected values for the chi-squared test. Red curves of the observed values and blue curves of the expected values for Shannon entropies, depending on each N value: (a) 98, (b) 212, (c) 398, (d) 596, (e) 810, and (f) 1040. The two curves (red and blue) become more similar to each other as N increases.

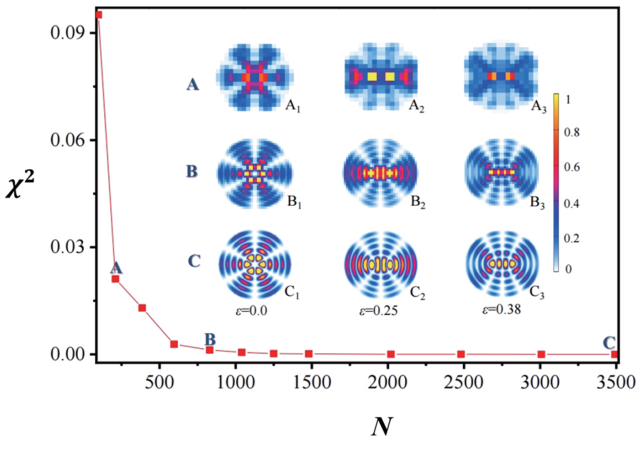

FIG. 4. The red squares for chi-squared test values are shown as N is varied. We set B (N = 810) to be the optimized minimum-mesh point for spatial resolution. Inset: $A_{1,2,3}$ is the mode pattern for N = 212 at ε = 0.0, 0.25, and 0.38, $B_{1,2,3}$ is the mode pattern for N = 810, and $C_{1,2,3}$ is the mode pattern for N = 3492. We can identify the quantum number (l = 5, m = 3) for B_1 as well as C_1.

ent. The criteria of the noticeable identification can be established, such that the local maximum of probability density for the mode pattern is larger than approximately the natural constant e multiplied by the local minimum value. That is, $\frac{\rho_{max}}{\rho_{min}} > e$. Consequentially, the optimized minimum-mesh point corresponds to the minimum resolution, and it can be used as a sampling of the morphology for the mode pattern.

When the number of mesh points N exceeds the saturated number (N = 3492), the morphologies of the mode patterns do not change and the resolution hardly increases (not shown in the figure). That is, we do not need N larger than the saturated number (N = 3492) to see the mode patterns clearly. This fact implies that the χ^2 value for the identifiable quantum numbers indicates the optimized minimum mesh size for the spatial resolution (minimum resolution), whereas the value for the saturation of the difference of Shannon entropies D_{SE} indicates the maximum mesh size for spatial resolution (maximum resolution).

4.3. Relation between Spatial Resolution and Increasing Wave Number

Intuitively, we can assume that the more massive the morphology of mode pattern becomes, the more mesh points we need for spatial resolution. To check this assumption, we investigate the relation between χ^2 and the eigenvalue trajectories of increasing Re(kR), since the increasing wave number Re(kR) directly makes the mode pattern more massive. Figure 5 shows these results. The red circles are for Re(kR)~2.8, the blue upward triangles are for Re(kR)~5.8, the green downward triangles are for Re(kR)~11.0, and the pink left-facing triangles are for Re(kR)~16.0. The absolute values of the curves for χ^2 increase as Re(kR) increases.

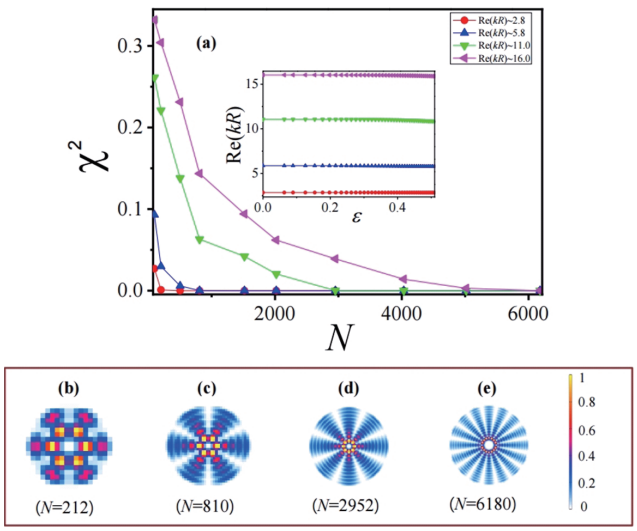

FIG. 5. Spatial resolution and increasing wave number. (a) χ^2 as a function of N. The red circles are for χ^2 Re(kR)~2.8, the blue upward triangles are for χ^2 Re(kR)~5.8, the green downward triangles are for χ^2 Re(kR)~11.0, and the pink left-facing triangles are for χ^2 Re(kR)~16.0. The absolute values of χ^2 increase as Re(kR) increases. The speed of convergence slows as the Re(kR) increases. The optimized minimum-mesh point for spatial resolution in (b) is N = 212, that in (c) is N = 810, that in (d) is N = 2952, and that in (e) is N = 6180. These optimized minimum-mesh points N_O are approximated as 2.2 × $(nkR)^2$.

Furthermore, the convergence rate becomes low as Re(kR) increases. That is, the optimized minimum-mesh point N_O for the red circles is N~212, for the blue upward triangles is N~810, for the green downward triangles is N~2952, and for the pink left-facing triangles is N~6180. These results match our intuition. At each optimized minimum mesh point N_O, we can identify the quantum numbers of the resonance-mode patterns in the circular resonator: The mode pattern of quantum numbers (l = 2, m = 3) is shown in Fig. 5(b); (l = 5, m = 3) is in Fig. 5(c); (l = 10, m = 4) is in Fig. 5(d); and (l = 13, m = 8) is in Fig. 5(e). From the results above, we can deduce a proportionality coefficient $\propto_N$ between the optimized minimum-mesh point N_O and $(nkR)^2$: $N_O \sim \{\propto_N \times (nkR)^2\}$ with $\propto_N$ ~2.2.

V. CONCLUSIONS

We study the Shannon entropy as an indicator of the spatial resolutions for the morphologies of the resonance-mode patterns in an elliptical resonator, and obtain two types of optimized mesh points of minimum and maximum size.

Using the chi-squared test, the optimized minimum-mesh size for spatial resolution can be confirmed by the identifiable quantum number. On the contrary, the saturation of difference in Shannon entropies can correspond to the optimized maximum-mesh size for spatial resolution, since after saturation the morphology of the mode pattern does not change and the resolution does not increase significantly.

We also investigate the relation between the optimized minimum-mesh point N_O for the chi-squared test and the increase in (real) wave number Re(kR) at constant refractive index n. The absolute values of the curves for chi-squared test values increase as the (real) wave number increases. Finally, we estimate the proportionality coefficient $\propto_N$ between the N_O and $(nkR)^2$, whose approximate value is 2.2. Note that the conditions we have studied cannot be directly applied to a chaotic resonator, since we only deal with an integrable resonator. In spite of this limitation, we hope that our results can be a cornerstone for research on both the morphologies of the mode patterns and their spatial resolutions from the perspective of information theory.

ACKNOWLEDGMENT

The Authors thank Kabgyun Jeong for valuable comments and support. This work was supported by Samsung Science and Technology Foundation under Project No. SSTP-BA1502-05, the National Research Foundation of Korea (Grant No. NRF-2020M3E4A1077861 & No.

2016R1D1A109918326 & No. 2020R1A2C3009299), and the Ministry of Science and ICT of Korea under ITRC program (Grant No. IITP-2019-0-01402).

REFERENCES

1. J. U. Nöckel, and A. D. Stone, "Ray and wave chaos in asymmetric resonant optical cavities," Nature **385**, 45–47 (1997).
2. C. Gmachl, F. Capasso, E. E. Narimanov, J. U. Nöckel, A. D. Stone, J. Faist, D. L. Sivco, and A. Y. Cho, "High-power directional emission from microlasers with chaotic resonators," Science **280**, 1556–1564 (1998).
3. S.-B. Lee, J. Yang, S. Moon, J.-H. Lee, K. An, J.-B. Shim, H.-W. Lee, and S. W. Kim, "Universal output directionality of single modes in a deformed microcavity," Phys. Rev. A **75**, 011802 (2007).
4. Q. H. Song, L. Ge, A. D. Stone, H. Cao, J. Wiersig, J.-B. Shim, J. Unterhinninghofen, W. Fang, and G. S. Solomon, "Directional laser emission from a wavelength-scale chaotic microcavity," Phys. Rev. Lett. **105**, 103902 (2010).
5. X. F. Jiang, Y. F. Xiao, C. L. Zou, L. He, C. H. Dong, B. B. Li, Y. Li, F. W. Sun, L. Yang, and Q. Gong, "Highly unidirectional emission and ultralow-threshold lasing from on-chip ultrahigh-Q microcavities," Adv. Mater. **24**, OP260–OP264 (2012).
6. S. M. Spillane, T. J. Kippenberg, and K. J. Vahala, "Ultralow-threshold Raman laser using a spherical dielectric microcavity," Nature **415**, 621–623 (2002).
7. S. Anders, W. Schrenk, E. Gornik, and G. Strasser, "Room-temperature operation of electrically pumped quantum-cascade microcylinder lasers," Appl. Phys. Lett. **80**, 4094–4096 (2002).
8. I. Teraoka, and S. Arnold, "Enhancing the sensitivity of a whispering-gallery mode microsphere sensor by a high-refractive-index surface layer," J. Opt. Soc. Am. B **23**, 1434–1441 (2006).
9. J. Zhu, S. K. Ozdemir, Y. F. Xiao, L. Li, L. He, D.-R. Chen and L. Yang, "On-chip single nanoparticle detection and sizing by mode splitting in an ultrahigh-Q microresonator," Nat. Photonics **4**, 46–49 (2009).
10. F. Bo, J. Wang, J. Cui, S. K. Ozdemir, Y. Kong, G. Zhang, J. Xu, and L. Yang, "Lithium-niobate–silica hybrid whispering-gallery-mode resonators," Adv. Mater. **27**, 8075–8081 (2015).
11. M. R. Foreman, D. Keng, E. Treasurer, J. R. Lopez, and S. Arnold, "Whispering gallery mode single nanoparticle detection and sizing: the validity of the dipole approximation," Opt. Lett. **42**, 963–966 (2017).
12. T. Nobis, E. M. Kaidashev, A. Rahm, M. Lorenz, and M. Grundmann, "Whispering gallery modes in nanosized dielectric resonators with hexagonal cross section," Phys. Rev. Lett. **93**, 103903 (2004).
13. S. Shinohara, M. Hentschel, J. Wiersig, T. Sasaki, and T. Harayama, "Ray-wave correspondence in limaçon-shaped semiconductor microcavities," Phys. Rev. A **80**, 031801 (2009).
14. J.-W. Ryu, and M. Hentschel, "Ray model and ray-wave correspondence in coupled optical microdisk," Phys. Rev. A **82**, 033824 (2010).
15. J. Kullig, and J. Wiersig, "Q spoiling in deformed optical microdisks due to resonance-assisted tunneling," Phys. Rev. E **94**, 022202 (2016).
16. S. Löck, A. Bäcker, R. Ketzmerick, and P. Schlagheck, "Regular-to-chaotic tunneling rates: from the quantum to the semiclassical regime," Phys. Rev. Lett. **104**, 114101 (2010).
17. E. J. Heller, "Bound-state eigenfunctions of classically chaotic hamiltonian systems: scars of periodic orbits," Phys. Rev. Lett. **53**, 1515 (1984).
18. S.-B. Lee, J.-H. Lee, J.-S. Chang, H-. J. Moon, S. W. Kim, and K. An, "Observation of scarred modes in asymmetrically deformed microcylinder lasers," Phys. Rev. Lett. **88**, 033903 (2002).
19. J. Wiersig, "Formation of long-lived, scarlike modes near avoided resonance crossings in optical microcavities," Phys. Rev. Lett. **97**, 253901 (2006).
20. J.-W. Ryu, S.-Y, Lee, and S.W. Kim, "Coupled nonidentical microdisks: avoided crossing of energy levels and unidirectional far-field emission," Phys. Rev. A **79**, 053858 (2009).
21. W. D. Heiss, "Repulsion of resonance states and exceptional points," Phys. Rev. E **61**, 929 (2000).
22. S.-B. Lee, J. Yang, S. Moon, S.-Y. Lee, J.-B. Shim, S. W. Kim, J.-H. Lee, and K. An, "Observation of an exceptional point in a chaotic optical microcavity," Phys. Rev. Lett. **103**, 134101 (2009).
23. L. Wang, D. Lippolis, Z. Y. Li, X.-F. Jiang, Q. Gong, and Y.-F. Xiao, "Statistics of chaotic resonances in an optical microcavity," Phys. Rev. E **93**, 040201 (2016).
24. X. Jiang, L. Shao, S.-X. Zhang, X. Yi, J. Wiersig, L. Wang, Q. Gong, M. Lončar, L. Yang, and Y.-F. Xiao, "Chaos-assisted broadband momentum transformation in optical microresonators," Science **358**, 344–347 (2017).
25. K.-W. Park, S. Moo, Y. Shin, J. Kim, K. Jeong, and K. An, "Shannon entropy and avoided crossings in closed and open quantum billiards," Phys. Rev. E **97**, 062205 (2018).
26. C. E. Shannon, "A mathematical theory of communication," Bell Syst. Tech. J. **27**, 379–423 (1948).
27. E.T. Jaynes, "Information theory and statistical mechanics," Phys. Rev. **106**, 620 (1957).
28. J. W. Godden, F. L. Stahura, and J. Bajorath, "Variability of molecular descriptors in compound databases revealed by shannon entropy calculations," J. Chem. Inf. Comput. Sci. **40**, 796–800 (2000).
29. B. J. Strait, and T. G. Dewey, "The shannon information entropy of protein sequences," Biophys. J. **71**, 148–155 (1996).
30. H. Zenil, S. Hernández-Orozco, N. A. Kiani, F. Soler-Toscano, A. Rueda-Toicen, and J. Tegnér, "A decomposition method for global evaluation of shannon entropy and local estimations of algorithmic complexity," Entropy **20**, 605 (2018).
31. R. González-Férez, and J. S. Dehesa, "Shannon entropy as an indicator of atomic avoided crossings in strong parallel magnetic and electric fields," Phys. Rev. Lett. **91**, 113001 (2003).
32. Y. L. He, Y. Chen, J. N. Han, Z. B. Zhu, G. X. Xiang, H. D. Liu, B. H. Ma, and D. C. He, "Shannon entropy as an indicator of atomic avoided crossings for Rydberg potassium atoms interacting with a static electric field," Eur. Phys. J. D **69**, 283 (2015).

33. F. Arranz, R.Benito, and F. Borondo, "Shannon entropy at avoided crossing in the quantum transition from order to chaos," Phys. Rev. E **99**, 062209 (2019).
34. J. Wiersig, "Boundary element method for resonances in dielectric microcavities," J. Opt. A **5**, 53 (2002).
35. A. M. Zhang, and Y. L. Liu, "Improved three-dimensional bubble dynamics model based on boundary element method," J. Comput. Phys. **294**, 208–223 (2015).
36. Z. Liu, S. Sun, A. H. D. Cheng, and Y. Wang, "A fast multipole accelerated indirect boundary element method for broadband scattering of elastic waves in a fluid-saturated poroelastic domain," Int. J. Numer. Anal. Methods Geomech. **42**, 2133–2160 (2018).
37. M. E. Gruber, and T. F. Eibert, "A hybrid Ewald-spectral cavity greens function boundary element method with spectral domain acceleration for modeling of over-moded cavities," IEEE Trans. Antennas Propag. **63**, 2627–2635 (2015).
38. I. Rotter, "A non-Hermitian Hamilton operator and the physics of open quantum systems," J. Phys. A: Math. Theor. **42**, 153001 (2009).
39. K.-W. Park, S. Moon, H. Jeong, J. Kim, and K. Jeong, "Non-hermiticity and conservation of orthogonal relation in dielectric microcavity," J. Phys. Commun. **2**, 075007 (2018).
40. R. A. Kullback, and R. A. Leibler, "On information and sufficiency," Ann. Math. Stat. **22**, 79–86 (1951).
41. J. N. Kapur, and H. K. Kesavan, "Entropy Optimization Principles and Their Applications," in *Entropy and energy dissipation in water resources*, V. P. Singh, M. Fiorentino. Ed. (Springer, Dordrecht, Nederlands. 1992), pp. 3–20.
42. R. L. Plackett, "Karl pearson and the chi-squared test," Int. Stat. Rev. **51**, 59–72 (1983).
43. F. Evers, and A. D. Mirlin, "Fluctuations of the inverse participation ratio at the Anderson transition," Phys. Rev. Lett. **84**, 3690 (2000).
44. N. C. Murphy, R. Wortis, and W. Atkinson, "Generalized inverse participation ratio as a possible measure of localization for interacting systems," Phys. Rev. B **83**, 184206 (2011).